

Shape Evolution of Cu₂O Nanostructures via Kinetic and Thermodynamic Controlled Growth

Choon Hwee Bernard Ng and Wai Yip Fan*

Department of Chemistry, National University of Singapore, 3 Science Drive 3, Singapore 117543

Received: March 24, 2006; In Final Form: August 21, 2006

We report the shape evolution process of Cu₂O nanocrystals upon slow oxidation of Cu under ambient conditions, yielding novel hexagonal and triangular platelike morphologies. The shape of the obtained nanocrystals evolves from hexagonal to triangular to octahedral; the growth patterns are governed by kinetically and thermodynamically controlled growth. Preferential adsorption of I[−] on {111} planes of Cu₂O nanoparticles induced the selective crystal growth of metastable platelike structures with {111} faces as the basal planes. On aging, the growth process appeared to shift into the thermodynamic regime and the thermodynamically stable octahedral shape is obtained. The possible growth mechanisms were investigated by varying the synthetic conditions. The band gap of Cu₂O nanooctahedrons was determined by the classical Tauc approach to be 2.24 eV, which is blue shifted with respect to the bulk Cu₂O value (2.17 eV). Results suggest that the slow oxidation process and use of crystallographic selective surfactants are essential for the appearance of anisotropic metastable shapes. In general, surface energy control by surfactant molecules might provide a convenient channel for tailoring nanocrystal shapes of metal oxides.

1. Introduction

Copper(I) oxide (Cu₂O) is a p-type semiconductor with a direct band gap of 2 eV and possesses unique optical and magnetic properties.^{1–3} Upon photoexcitation, the excitons of Cu₂O are found to be long-lived (10 μs) and there is evidence to suggest that their motion through the solid can be coherent, in a manner analogous to photon coherence in lasers.⁴ In addition, Cu₂O has attracted much interest due to its potential applications in solar energy conversion, nanoelectronics, magnetic storage devices, catalysis, and biosensing.^{5–7} It was reported that Cu₂O microspheres can be used as the negative electrode material for lithium-ion batteries⁸ and as a stable catalyst for photochemical decomposition of water into O₂ and H₂ under visible light irradiation.⁹ Recently, there have been great efforts in the shape-controlled synthesis of Cu₂O nanocrystals since shape is known to be an important factor in determining the structural, physical, and chemical properties of nanoparticles.^{10,11}

Various methods have been reported for the production of Cu₂O nanocrystals with varied morphologies: monodispersed nano- and microcubes were prepared by Murphy et al. from the reduction of Cu(II) salts in the presence of poly(ethylene) glycol (PEG, $M_w = 600$) and cetyltrimethylammonium chloride (CTAB) as protecting agents.^{12,13} Using poly(vinyl pyrrolidone) (PVP) as the capping agent, Xie et al. obtained submicrometer octahedrons,¹⁴ while nanooctahedrons with controllable sizes in the range of ~100 nm have been prepared via γ irradiation in Triton X-100 microemulsions¹⁵ as well as via reduction of Cu(OH)₂ with hydrazine.¹⁶ Hollow spheres (300–600 nm) can be formed in the presence of deionized gelatin as soft templates.^{17,18} In addition, electrodeposition methods^{19,20} are commonly used to synthesize one-dimensional nanowires and nanorods, which have also been obtained via solution methods using PEG ($M_w = 20\,000$) and double-chain cationic lipid templates.^{21,22}

In our work, single-crystalline Cu₂O nanostructures of various novel morphologies (hexagonal, triangular plates, and octahedrons) have been synthesized using a simple solution-phase route under ambient conditions. Oxidation of copper (Cu) colloids for different periods of time in the presence of I[−] yielded Cu₂O nanoparticles of different shapes, and their properties were characterized by UV–visible absorption spectroscopy, transmission electron microscopy (TEM), high-resolution transmission electron microscopy (HRTEM), scanning electron microscopy (SEM), powder X-ray diffraction (XRD), and energy-dispersive X-ray analysis (EDX).

2. Experimental Section

Reagent-grade chemicals were obtained from Sigma Aldrich and used without further purification. Cu nanoparticles were synthesized using a solution-phase procedure adapted from a previously reported method.²³ A 10 mL amount of an aqueous solution of copper sulfate (CuSO₄·5H₂O, 10^{−3} M) and potassium iodide (KI, 10^{−3} M) was bubbled with argon for 15 min in a volumetric flask. Next, 10 mL of deaerated sodium borohydride (NaBH₄, 6 × 10^{−3} M) was added in ~2 mL aliquots with vigorous shaking after each addition. The above step was performed in the presence of air. On standing for 5 min, a deep-red Cu colloidal solution was obtained. The solution was then exposed to air further, giving a yellow solution after ~2 h, and allowed to age for up to 3 days. The particles were then separated from the solutions by centrifugation at 5000 rpm for 20 min and resuspended in water. The process was repeated twice to remove the excess surfactant. The precipitate was collected and redispersed in a small amount of deionized water for characterization. Control experiments were performed by replacing KI with sodium chloride (NaCl, 10^{−3} M), potassium bromide (KBr, 10^{−3} M), trisodium citrate (Na₃Cit, 10^{−3} M), and PVP (10^{−3} M).

The progress of the oxidation was followed by a UV–visible absorption spectrometer (Shimadzu UV-2550). Aliquots of the reaction mixture were retrieved at various oxidation times for

* To whom correspondence should be addressed. Fax: 6567791691. E-mail: chmfanwy@nus.edu.sg.

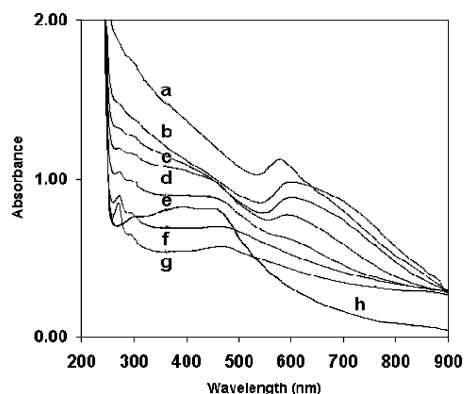


Figure 1. UV-visible absorption spectra of reaction mixture at various times of oxidation accompanying a change in particle morphology of the Cu_2O nanocrystals: (a) 30, (b) 60, (c) 90, (d) 120, (e) 150, (f) 180, and (g) 210 min and (h) after aging for 3 days.

TEM and EDX analyses. TEM images (JEOL-2010 or JEOL-3010) were taken from direct sampling of the solution on carbon-coated copper grids, and EDX spectra were taken during the TEM (JEOL-3010) imaging process. SEM microscopy imaging was performed on Cu_2O samples deposited on silicon plates using a JEOL JSM-6700F field emission instrument. XRD patterns were recorded from a powder Cu_2O sample supported on a glass slide using a SIEMENS D5005 diffractometer ($\text{Cu K}\alpha$, $\lambda = 0.15418 \text{ nm}$) at a scanning rate of 0.01 deg s^{-1} for 2θ in the range from 20° to 80° .

3. Results and Discussion

Oxidation of Cu nanoparticles to Cu_2O nanostructures was monitored by UV-visible absorption spectroscopy (Figure 1). At the initial stage there is an absorption band centered at 565 nm. This corresponds to the plasmon absorbance band of Cu nanoparticles. After 30 min of exposure to air, a weak exciton absorption peak emerges at $\sim 700 \text{ nm}$, which ends with formation of Cu_2O nanoclusters. The two bands appear to overlap, giving a broad absorption from 600 to 800 nm with a gradually decreasing intensity over time, indicating depletion of Cu nanoparticles. Complete disappearance of the 600–800 nm absorption after 180 min coincides with the appearance of a sharp peak at $\sim 270 \text{ nm}$, suggesting a distinct change in particle morphology. The intensity of the 270 nm peak increases from 180 to 210 min accompanied by the appearance of a much weaker band at $\sim 470 \text{ nm}$. On aging of the reaction mixture for up to 3 days, there is a red shift in the ~ 270 and $\sim 470 \text{ nm}$ bands to ~ 300 and $\sim 490 \text{ nm}$, respectively. A decrease in intensity for the former and an increase in intensity for the latter were observed. Previous work has illustrated a shift in the absorption toward higher energy with a decrease in the size of cuprous oxide nanocrystals.²⁴ The red shift in the absorption with aging time may thus be attributed to an increase in the size of the crystals. The oxidation process was accompanied by a color change from red to blue to green to yellow. Finally, orange crystals were obtained on aging.

Cu_2O nanostructures at various stages of the growth process were characterized by TEM. Figure 2 shows the images of the sample taken from the reaction mixture after the solution was exposed to air for 0, 30, 90, 150, and 210 min and after an aging period of 3 days. Due to the quick reduction process, $\sim 10 \text{ nm}$ spherical Cu nanoparticles were formed immediately in the initial reaction mixture (Figure 2a). At 30 min, small spherical Cu_2O nanoclusters were dominant while a few $\sim 40 \text{ nm}$ faceted Cu_2O nanostructures appeared in the mixture (as

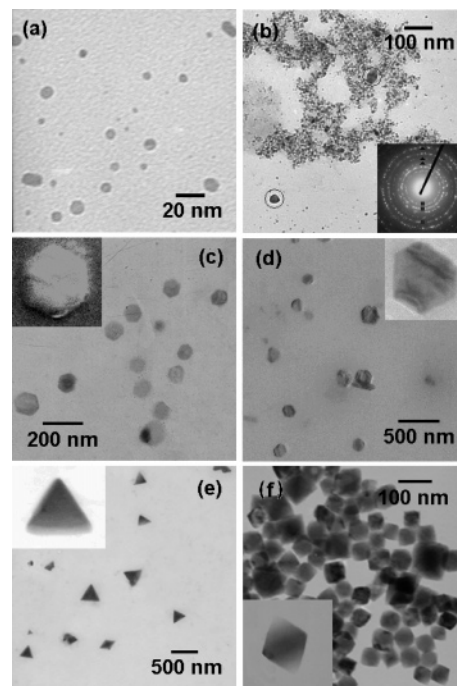


Figure 2. TEM images of the sample after various times of oxidation: 0, 30, 90, 150, and 210 min and after an aging period of 3 days. (a) Cu nanoparticles, (b) faceted Cu_2O nanocrystals, (c) hexagonal nanoplates, (d) truncated nanoprisms, (e) triangular nanoplates, and (f) octahedral nanocrystals.

circled in Figure 2b). Electron diffraction of the particles gave rings arising from both Cu and Cu_2O (inset of Figure 2b; square, Cu_2O ; triangle, Cu). These nanoclusters would serve as seeds for the growth of Cu_2O nanoplates. At 90 min, the reaction mixture became blue-green; most particles in the mixture were 40–60 nm hexagonal nanoplates (Figure 2c). Truncated nanoprisms (Figure 2d) were observed at 150 min when the solution turned yellow-green, and the products after 210 min were uniform triangular nanoplates (Figure 2e). An aging period of 3 days resulted in transformation of the triangular nanoplates to octahedral nanocrystals (Figure 2f). The difference in the contrast between the equatorial part and the polar part suggests its octahedral morphology. Figure 3 shows the statistical analyses of the respective nanocrystals obtained from counting ~ 100 nanoparticles for each sample. The average size of each nanocrystal shape was calculated from the center of a Gaussian distribution.

The TEM observations and UV-visible absorption spectra describe a clear growth process. The initial stage (0–30 min) is a seed formation process in which the size of the particles changes very slowly; at the intermediate stage (30–90 min), the seeds formed in the initial stage quickly grew to hexagonal nanoplates. As the reaction proceeds (90–210 min), further growth of the hexagonal nanoplates led to the appearance of triangular nanoplates. The Cu_2O triangular nanoplates were believed to grow via Ostwald ripening in which large crystals grow at the expense of small ones, leading to the observed wide size distribution (Figure 3). The reaction can be ceased at various times to obtain crystals of a particular morphology by removing the crystals from the reaction mixture by centrifugation.

Figure 4a gives the TEM image of the Cu nanoparticles ($\sim 10 \text{ nm}$) before oxidation. The SAED of the sample gave rings that could be indexed to diffraction planes of fcc Cu (Figure 4b). On oxidation, Cu_2O nanoplates with hexagonal and triangular morphologies were obtained. The hexagonal nanoplates were uniform single crystals with an average edge length of 43 nm

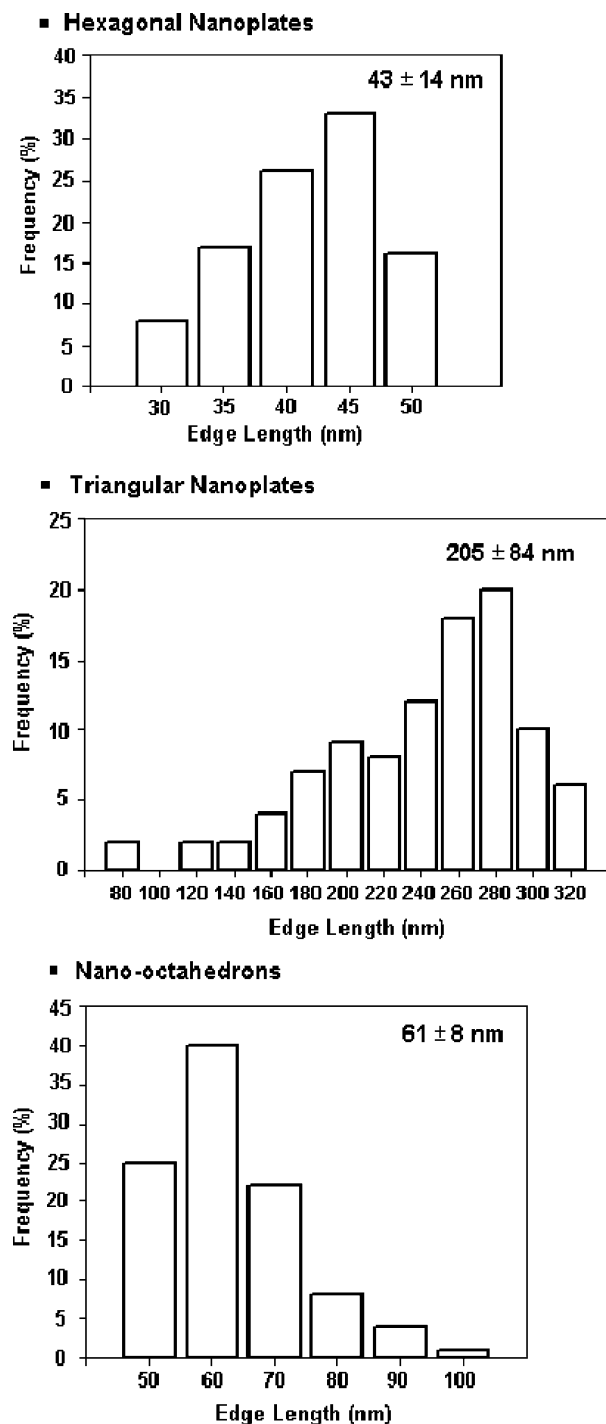


Figure 3. Size distribution (edge-length) histograms of Cu₂O products.

(Figure 5a). Figure 5b and 5c gives the TEM image of a single hexagonal nanoplate and the electron diffraction pattern obtained by aligning the electron beam perpendicular to the planar surface of the nanoplates. The 6-fold symmetry of the diffraction spots indicates that the hexagonal faces are bound by {111} planes.²⁵ Two sets of spots can be identified based on their *d* spacing: spacings of 1.17 and 1.50 Å are due to the (222) and (220) Bragg reflections of cubic Cu₂O, respectively. HRTEM imaging of a nanocrystal shows visible lattice fringes (Figure 5d) which indicate that the nanoparticle is a single crystal. The *d* spacing is about 2.18 Å, corresponding to the {200} plane of cubic Cu₂O.

Figure 6a shows that the triangular nanoplates were also uniform single crystals with an average edge length of 205 nm.

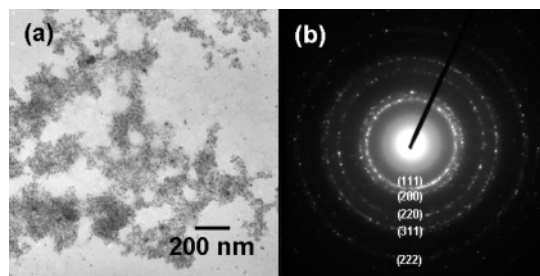


Figure 4. (a) TEM image of Cu nanoparticles. (b) SAED pattern obtained which consists of rings that could be indexed to face-centered cubic Cu.

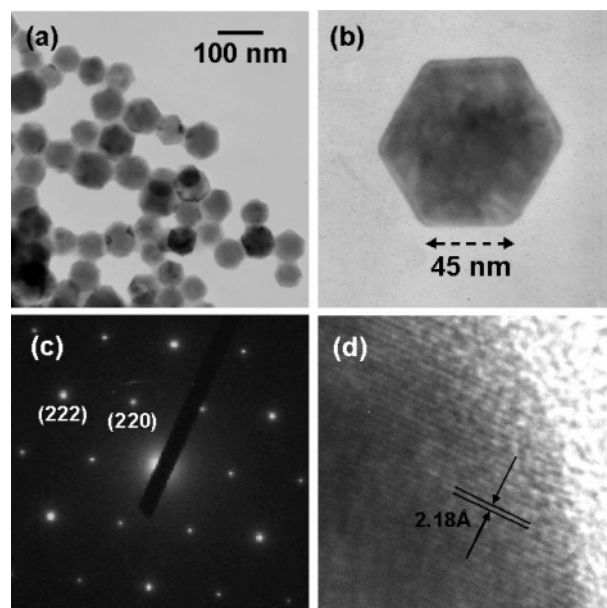


Figure 5. (a) TEM image of Cu₂O hexagonal nanoplates. (b) Single hexagonal nanoplate. (c) SAED pattern obtained from a single hexagonal nanoplate. (d) HRTEM image of hexagonal nanoplate.

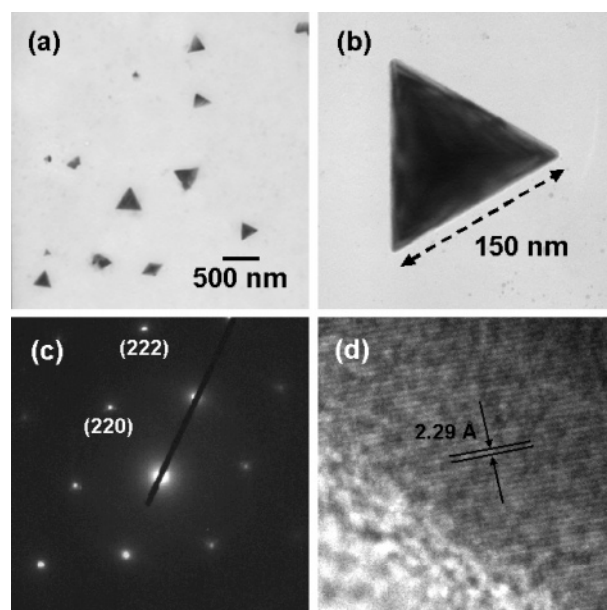


Figure 6. (a) TEM image of Cu₂O triangular nanoplates. (b) Single triangular nanoplate. (c) SAED pattern obtained from a single triangular nanoplate. (d) HRTEM image of triangular nanoplate.

Similar to the case of the hexagonal nanoplate, the electron diffraction pattern obtained by aligning the electron beam perpendicular to the planar surface of the a single triangular

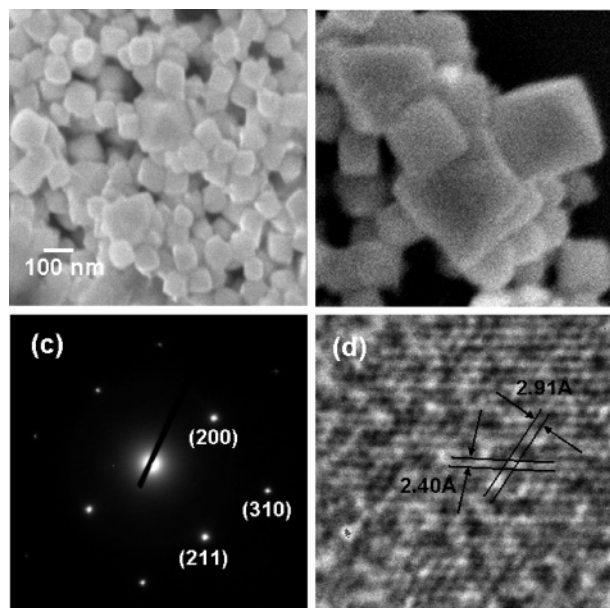


Figure 7. (a) SEM image of Cu_2O nanooctahedrons. (b) SEM image of larger crystals revealing its octahedral morphology. (c) SAED pattern obtained from a single nanooctahedron. (d) HRTEM image of a nanooctahedron.

nanoplate shows a 6-fold rotational symmetry of the diffraction spots (Figure 6c), which indicates that these nanoplates are single

crystals with a (111) lattice plane as the basal plane.²⁵ Two sets of spots can be identified based on their d spacing: spacings of 1.21 and 1.45 Å are due to the (222) and (200) Bragg reflections of cubic Cu_2O , respectively. Visible lattice fringes were observed in HRTEM (Figure 6d) with d spacing of about 2.29 Å, corresponding to the {111} plane of cubic Cu_2O .

On aging of the reaction mixture octahedral Cu_2O nanocrystals with an average side length of 61 nm were obtained (Figure 7a). The octahedral morphology may be observed in SEM images of larger crystals as shown in Figure 7b. Electron diffraction of an octahedral nanocrystal reveals three sets of spots (Figure 7c); The d spacings of 1.34, 1.76, and 2.08 Å are due to the (310), (211), and (200) Bragg reflections of cubic Cu_2O , respectively. The high-resolution transmission electron microscopy (HRTEM) image of a nanocrystal in Figure 7d shows visible lattice fringes with d spacings of about 2.40 and 2.91 Å corresponding to the {111} and {110} planes of cubic Cu_2O , respectively.

The identity of the octahedral nanoparticles was shown to be cuprite Cu_2O by EDX and XRD. EDX analysis gave peaks due to Cu and O only as well as elemental ratios of Cu:O of ~2:1 (Figure 8a). Powder X-ray diffraction (XRD) patterns of the as-prepared Cu_2O samples (Figure 8b) revealed formation of a single cubic phase Cu_2O with a cubic cuprite structure (JCPDF #00-005-0667). No other diffraction peaks arising from metallic Cu or CuO appear in the XRD pattern. The high intensity of the {111} diffraction peak suggests that the

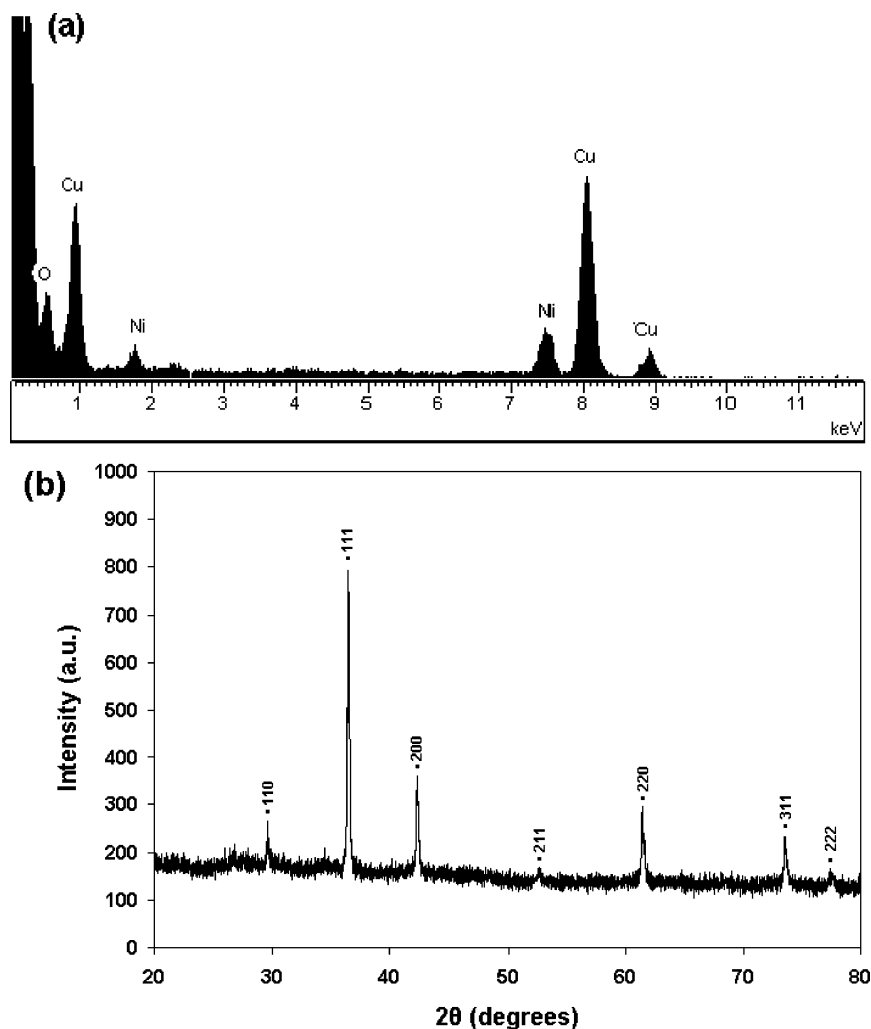


Figure 8. (a) EDX and (b) XRD of Cu_2O cubic nanoparticles. The Ni signals of the EDX plots belong to the nickel grid used for nanoparticle deposition. The XRD peaks are indexed to cuprite Cu_2O .

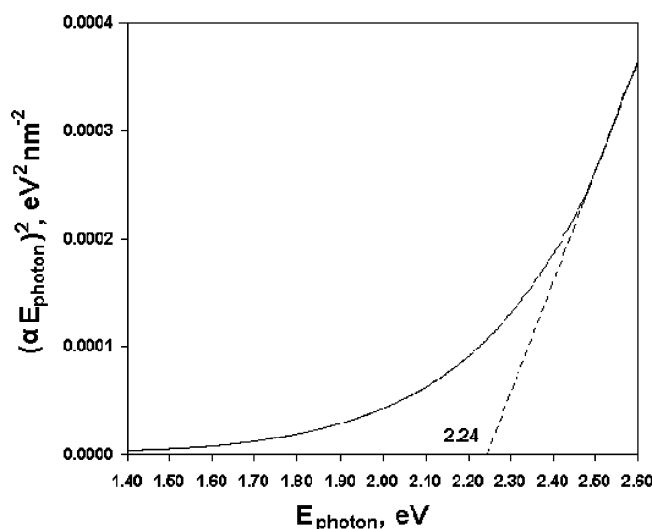


Figure 9. Plot of $(\alpha E_{\text{photon}})^2$ against E_{photon} for a direct transition.

nanocrystals are mainly dominated by $\{111\}$ facets, and the $\{111\}$ planes tend to be preferentially oriented parallel to the surface of the supporting substrate.

For semiconductors the absorption of photons with energy similar to that of the band gap, $h\nu \approx E_g$, leads to an optical transition producing an electron in the conduction band and a hole in the valence band (exciton). Such an electronic transition is subject to the selection rule such that the wave vector (k) must be conserved (i.e., $\Delta k = 0$). Semiconductors such as Cu₂O, in which the wave vector is conserved for optical transitions, are known as direct band gap semiconductors and have large absorption coefficients. From the UV–visible absorption spectra of Cu₂O nanooctahedrons (Figure 1h) a broad absorption band can be seen from 300 to 450 nm. A classical Tauc approach was employed to estimate their optical energy band gaps using the following equation for a semiconductor²⁶

$$\alpha(\nu) = A(h\nu/2 - E_g)^{m/2}$$

where A is a constant, α is the absorption coefficient, and m equals 1 for a direct transition. Assuming that all 10^{-3} M CuSO₄ has been fully converted into Cu₂O nanocrystals, the concentration of Cu₂O in colloidal form (C) would be 0.0715 g/L. This corresponds to an effective thickness $d = 119$ nm by the following formula: $d = (lC/\rho)$, where l is the optical path length ($=10$ mm) and ρ is the Cu₂O density ($=0.006$ g/mm³). Figure 9 shows a plot of $(\alpha E_{\text{photon}})^2$ against E_{photon} for a direct transition, where the absorption coefficient $\alpha = (\text{absorbance})/d$. The value of $(\alpha E_{\text{photon}})^2$ extrapolated to $\alpha = 0$ gives an absorption edge of 2.24 eV, corresponding to the band gap E_g of Cu₂O nanooctahedrons. The blue shift in E_g of the nanooctahedrons with respect to bulk Cu₂O (2.17 eV) is the result of quantum-confinement effects arising from the small size regime.^{27,28}

In our case, the iodide ion I^- is believed to play multiple roles besides being used as a protective agent against aggregation. Strong affinity between Cu(I) and I^- accounts for the formation and stabilization of nanoscale Cu₂O, preventing its facile oxidation to CuO as in the bulk situation.²⁹ According to the hard–soft acid base (HSAB) theory, I^- is a soft Lewis base and Cu^+ is a soft Lewis acid, leading to a favorable mutual affinity. Cu^{2+} is a borderline Lewis acid; therefore, its interactions with I^- are predicted to be weak. In a basic environment

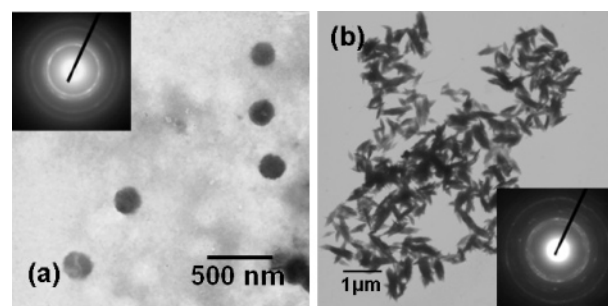
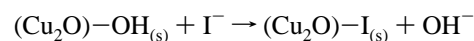


Figure 10. (a) Polycrystalline Cu₂O spherical nanoparticles obtained with PVP as the protecting agent. (b) Cu₂O nanoflakes obtained with Br[−] as the protecting agent. (Inset) Electron diffraction of the respective products, both of which can be indexed to cuprite Cu₂O.

TABLE 1: Summary of the Experimental Observations with Different Surfactants

surfactant	color of crystals	product morphology
Cl [−]	black	clusters with no definite morphology
Br [−]	black	flakes (Figure 10b)
citrate	green	clusters with no definite morphology
PVP	yellow	spheres (Figure 10a)

(due to excess NaBH₄), I^- adsorption occurs by substitution of surface hydroxyl groups of Cu₂O by I^- ³⁰



The surface-adsorbed I^- and the counterions (Na^+ or K^+) create an electrical double layer, which is responsible for generating a repulsive interaction between the Cu nanoparticles, affording electrostatic stabilization against aggregation. To investigate the effect of surfactants on the Cu₂O nanocrystal shapes, control experiments were performed in which NaCl, KBr, Na₃Cit, and PVP were used as the protecting agent. As summarized in Table 1, use of PVP gave spherical polycrystalline Cu₂O nanoparticles embedded in the polymer matrix (Figure 10a) while the presence of Br[−] resulted in the appearance of Cu₂O nanoflakes (Figure 10b). Both Cl[−] and Cit^{3−} were unable to afford electrostatic stabilization against aggregation, leading to formation of Cu₂O clusters with no definite morphology. This indicates that I^- plays an important role in inducing the formation of the $\{111\}$ planes to facilitate the growth of nanoplates and is essential to the shape evolution process. This special property of I^- is probably a result of soft acid–soft base affinity which correlates with our observations that Br[−] (a moderate soft base) resulted in anisotropic growth but not to the extent of highly faceted nanocrystals while Cl[−] and Cit^{3−} (hard bases) could not coordinate well enough with Cu₂O to form nanocrystals with definite shapes.

To determine the influence of light in the shape evolution process, experiments were performed in the presence of light as well as in the dark. However, the outcome did not vary greatly, suggesting that light was not a determining factor in the formation of anisotropic nanostructures as in the case of Ag.³¹

Figure 11 shows a schematic illustration of a possible mechanism for the formation and evolution of nanocrystals of different morphologies, governed by the delicate balance between kinetic and thermodynamic growth regimes. At the initial stages of the reaction nonequilibrium growth conditions (high monomer concentrations, slow oxidation, and low temperatures) drive the growth process into the kinetic growth regime where selective growth on high-energy crystallographic facets is facilitated and transient species are formed. In this

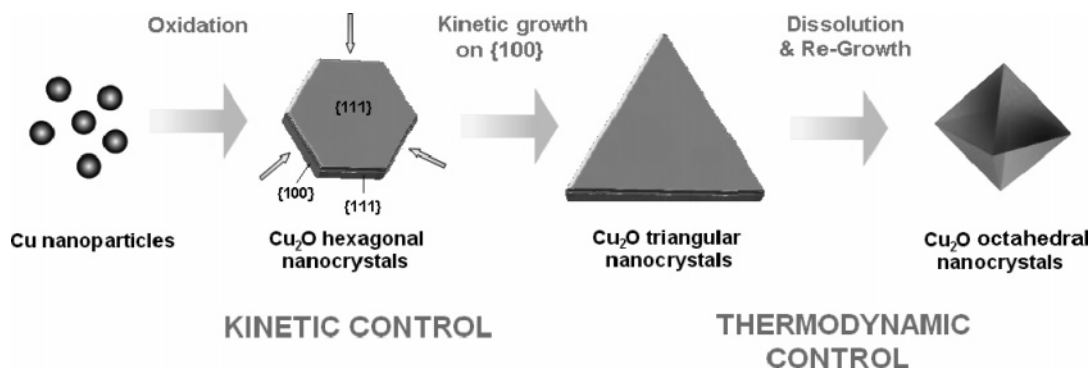


Figure 11. Scheme for the growth of nanocrystals with different morphologies. Arrow indicates the diffusion directions of the monomers.

regime kinetic control is possible by selective adsorption of surfactants on different crystallographic facets, resulting in modification of the surface free energy of individual crystallographic facets, leading to formation of anisotropic nanoplates.^{10,32,33}

On the basis of our observations, I[−] may be specific for binding to {111} facets. The dominant adsorption of I[−] on the {111} facets lowers the energy of these facets and drives the growth of nuclei in a 2D mode to produce hexagonal nanoplates with confined {111} planes. The appearance of hexagonal platelike morphologies is still unclear but may arise from the crystalline phase of the seeds during nucleation influenced by its characteristic unit cell structure.³⁴ Previous studies on cubic-structured hexagonal nanoplates have shown that the side faces of a hexagonal nanoplate are bound by a mix of {100} and {111} planes.^{25,35,36} It is therefore not unreasonable to assume a similar situation in our case. Passivation of the {111} facets by I[−] adsorption leads to a higher growth rate on the three {100} sides, resulting in the evolution of hexagonal to triangular nanoplates (Figure 11). Preferential growth on three alternate planes was also used to account for the shape evolution of Ag polygons to triangular nanostructures.³⁷

Another important aspect of this synthesis lies in the presence of excess NaBH₄, which led to a slow oxidation process and ultimately slow formation of Cu₂O nanocrystals. When Cu₂O nanocrystals are formed at a sufficiently high rate, the final product will have no choice but to assume the thermodynamically favored shape, which is the octahedron. However, when the oxidation becomes substantially slow, nucleation and growth may be kinetically controlled and the final product can take shapes deviating from the thermodynamic ones.

On aging, the growth process shifts into the thermodynamic growth regime due to the low flux of monomers. Thermodynamic growth is governed by the Gibbs–Curie–Wulff theorem, which suggests that the shape of a crystal is determined by the relative surface free energy of individual crystallographic faces. The final crystal shape results from minimizing the total free energy of the system.³⁸ In our case, the triangular nanoplates convert to the thermodynamically favored uniform octahedral nanoparticles by dissolution and regrowth of monomers (Figure 12a). Such a phenomenon has also been observed in the shape evolution of titania nanocrystals.³⁹ Surfaces of spherical single-crystalline particles contain high-index crystallography planes resulting in a high surface energy. Hence, facets tend to form on the particle surface to increase the portion of the low-index planes so as to minimize the total surface energy, leading to the appearance of cubooctahedral shapes with stable {100} and {111} facets.⁴⁰ There were no further change in morphology on aging for longer periods of time, but hollow interiors were observed to form in some nanooctahedrons. (Figure 12b)

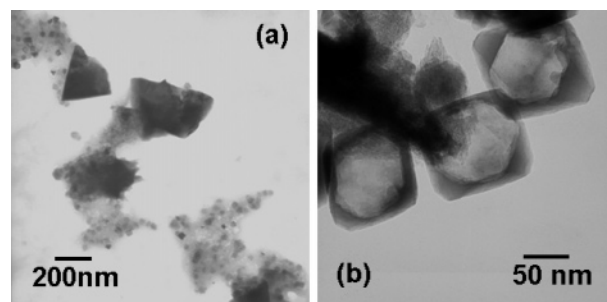


Figure 12. (a) TEM images showing the dissolution of Cu₂O triangular nanoplates to smaller octahedral nanocrystals. (b) TEM image of hollow octahedral nanocrystals.

Thermodynamically, all of the nanocrystals will grow toward the shape having the lowest energy at equilibrium, which is governed by the classic theory. However, the formation kinetics can affect the shape of the formed nanocrystals and metastable nanocrystal shapes such as hexagonal and triangular nanoplates can be arrested before the reaction reaches the equilibrium stage by tuning the reaction conditions. Experimentally this is done by quenching the growth process at appropriate times by removing the crystals from solution via centrifugation.

The mechanism of hollow interior growth in nanooctahedrons is still unclear, but the common mechanisms for generation of interior space, Ostwald ripening and Kirkendall effect, were ruled out. Ostwald ripening is normally responsible for formation of hollow interiors in colloidal aggregates made up of nanocrystallites. Owing to the inhomogeneous size and distribution of crystallites within the aggregates, large crystallites are almost immobile while the smaller ones undergo mass relocation through dissolution and regrowth, creating the interior space within the original aggregates. However, in our case, both the hollow nanocrystals and its solid counterparts showed no indications of polycrystallinity for Ostwald ripening to operate. On the other hand, the Kirkendall effect operates in systems where a diffusion couple is present, resulting in a composition change of the initial and final crystals. In the formation of hollow nanooctahedrons we did not detect a change in chemical composition and no core–shell intermediates were observed, thus ruling out its possibility.

4. Conclusion

We have shown that the slow oxidation of Cu in the presence of I[−] under ambient conditions yielded Cu₂O nanocrystals with novel hexagonal and triangular platelike morphologies. This was achieved by controlling the relative rates of growth of various crystal planes by crystallographically selective adsorption of the protective agent I[−], inducing growth of metastable platelike structures. On aging, the growth process appears to shift into

the thermodynamic regime and the thermodynamically stable octahedral shape is obtained. The band gap of Cu₂O nano-octahedrons was determined by the classical Tauc approach to be 2.24 eV, which is blue shifted with respect to the bulk Cu₂O value (2.17 eV). The large anisotropy of these hexagonal and triangular nanoplates should substantially influence or even enhance their optical properties (e.g., light absorption and scattering and surface-enhanced Raman spectroscopy (SERS)), and these Cu₂O nanostructures may find potential applications in solar energy conversion and catalysis and as model systems for fundamental research.

Acknowledgment. The project was supported by the Agency of Science, Technology and Research (ASTAR) under Grant No.143-000-198-305 and a National University of Singapore grant 143-000-298-112. We thank B. Liu and G. L. Loy for their help with TEM microscopy.

References and Notes

- Grozdanov, I. *Mater. Lett.* **1994**, *19*, 281.
- Shen, M. Y.; Yokouchi, T.; Koyama, S.; Goto, T. *Phys. Rev. B* **1997**, *56*, 13066.
- Shi, W.; Lim, K.; Liu, X. *J. Appl. Phys.* **1997**, *81*, 2822.
- Snoke, D. *Science* **1996**, *273*, 1351.
- Briskman, R. N. *Sol. Energy Mater. Sol. Cells* **1992**, *27*, 361.
- Li, X.; Gao, H.; Murphy, C. J.; Gou, L. *Nano Lett.* **2004**, *4*, 1903.
- Liu, R.; Kulp, E. A.; Oba, F.; Bohannon, E. W.; Ernst, F.; Switzer, J. A. *Chem. Mater.* **2005**, *17*, 725.
- Poizot, P.; Laruelle, S.; Grugeon, S.; Dupont, L.; Taron, J. M. *Nature* **2000**, *407*, 496.
- Hara, M.; Kondo, T.; Komoda, M.; Ikeda, S.; Shinohara, K.; Tanaka, A.; Kondo, J. N.; Domen, K. *Chem. Commun.* **1998**, 357.
- Puntes, V. F.; Krishnan, K. M.; Alivisatos, A. P. *Science* **2001**, *291*, 2115.
- Sun, Y. G.; Xia, Y. N. *Science* **2002**, *298*, 2176.
- Gou, L.; Murphy, C. J. *J. Mater. Chem.* **2004**, *14*, 735.
- Gou, L.; Murphy, C. J. *Nano Lett.* **2003**, *3*, 231.
- Zhang, X.; Xie, Y.; Xu, F.; Liu, X. H.; Xu, D. *Inorg. Chem. Commun.* **2003**, *6*, 1390.
- He, P.; Shen, X.; Gao, H. *J. Colloid Interface Sci.* **2005**, *284*, 510.
- Xu, H.; Wang, W.; Zhu, W. *J. Phys. Chem. B* **2006**, *110*, 13829.
- Yang, M.; Zhu, J. *J. Cryst. Growth* **2003**, *256*, 134.
- Xu, L.; Chen, X.; Wu, Y.; Chen, C.; Li, W.; Pan, W.; Wang, Y. *Nanotechnology* **2006**, *17*, 1501.
- Ko, E.; Choi, J.; Okamoto, K.; Tak, Y.; Lee, J. *ChemPhysChem* **2006**, *7*, 1505.
- Lee, Y. H.; Leu, I. C.; Liao, C. L.; Chang, S. T.; Wu, M. T.; Yen, J. H.; Fung, K. Z. *Electrochem. Solid-State Lett.* **2006**, *9*, A207.
- Wang, W.; Wang, G.; Wang, X.; Zhan, Y.; Liu, Y.; Zheng, C. *Adv. Mater.* **2002**, *14*, 67.
- Paradies, H. H.; Thies, M.; Hinze, U. *Rigaku J.* **2000**, *17*, 9.
- Kapoor, S.; Joshi, R.; Mukherjee, T. *Chem. Phys. Lett.* **2002**, *354*, 443.
- Borgohain, K.; Murase, N.; Mahamuni, S. *J. Appl. Phys.* **2002**, *92*, 1292.
- Xiong, Y.; McLellan, J. M.; Chen, J.; Yin, Y.; Li, Z. Y.; Xia, Y. *J. Am. Chem. Soc.* **2005**, *127*, 17118.
- Tsunekawa, S.; Fukuda, T.; Kasuya, A. *J. Appl. Phys.* **2000**, *87*, 1318.
- Wang, E. M.; Searson, P. C. *Appl. Phys. Lett.* **1999**, *74*, 2939.
- Murray, C. B.; Norris, D. J.; Bawendi, M. G. *J. Am. Chem. Soc.* **1993**, *115*, 8706.
- Ram, S.; Mitra, C. *Mater. Sci. Eng.* **2001**, *805*, A304.
- Lefevre, G.; Walcarius, A.; Ehrhardt, J. J.; Bessiere, J. *Langmuir* **2000**, *16*, 4519.
- Jin, R.; Cao, C. Y.; Hao, E.; Metraux, G. S.; Schatz, G. C.; Mirkin, C. A. *Nature* **2003**, *425*, 487.
- Puntes, V. F.; Zanchet, D.; Erdonmez, C. K.; Alivisatos, A. P. *J. Am. Chem. Soc.* **2002**, *124*, 12874.
- Bradley, J. S.; Tesche, B.; Busser, W.; Maase, M.; Reetz, M. T. *J. Am. Chem. Soc.* **2000**, *122*, 4631.
- Alivisatos, A. P. *J. Phys. Chem.* **1996**, *100*, 13226.
- Maillard, M.; Giorgio, S.; Pileni, M. P. *Adv. Mater.* **2002**, *14*, 1084.
- Germain, V.; Li, J.; Ingert, D.; Wang, Z. L.; Pileni, M. P. *J. Phys. Chem. B* **2003**, *107*, 8717.
- Tian, X.; Chen, K.; Cao, G. *Mater. Lett.* **2006**, *60*, 828.
- Mullin, J. W. *Crystallization*, 4th ed.; Butterworth Heinemann: Boston, 2001.
- Jun, Y.; Casula, M. F.; Sim, J.; Kim, S. Y.; Cheon, J.; Alivisatos, A. P. *J. Am. Chem. Soc.* **2003**, *125*, 15981.
- Wang, Z. L. *J. Phys. Chem. B* **2000**, *104*, 1153.